Epitaxial inorganic metal-halide perovskite films with controlled surface terminations

Janek Rieger, Tilman Kißlinger, Andreas Raabgrund, Jonas Hauner, Daniel Niesner,
M. Alexander Schneider, and Thomas Fauster[*]

Lehrstuhl für Festkörperphysik, Friedrich-Alexander-Universität Erlangen-Nürnberg (FAU), Staudtstrasse 7, 91058 Erlangen, Germany

Metal-halide perovskite (MHP) thin films for next-generation solar cells are typically fabricated by wet-chemical synthesis in which surface properties such as the orientation of surface facets and their termination cannot be controlled. MHP device efficiencies depend critically on those surface properties. We demonstrate the epitaxial growth of several nanometer thick purely (001)-oriented films of $CsPbBr_3$ and $CsSnBr_3$ MHPs on Au(001) by molecular beam epitaxy. The epitaxial films are in a cubic phase aligned with the substrate. Their surfaces are singly terminated and can be modified for the first time. While the CsBr and $PbBr_2$ surface terminations differ in terms of their atomic structure and defect content, the films are intrinsic semiconductors irrespective of the termination. The work function of the $PbBr_2$-terminated surface is increased by 0.7 eV, which has drastic implications for the level alignment at MHP interfaces.

I. INTRODUCTION

The rapid progress in the development of thin-film solar cells based on metal-halide perovskites (MHPs) has motivated intense research [1]. The optimization of devices was achieved by improving the MHP film morphology, mitigating defects in the bulk and at interfaces. For a high device efficiency, the interface level alignment is crucial and depends on a detailed understanding of the involved internal surfaces [2,3]. In particular, the surface orientation and defects play major roles [4,5]. Surface properties such as work function and ionization energy are frequently used to presume the interface level alignment [6]. These presumptions are only valid if the surface structure is well known and can be prepared reproducibly. For optimal solar-cell efficiencies, well-defined MHP surfaces with (001) orientation may be beneficial [4,7]. A desirable but hitherto not demonstrated way to fulfill all requirements would be the epitaxial layer-by-layer growth of MHPs with only one domain in (001) orientation [2].

The exceptional device performance of MHPs relies on ultralong lifetimes of charge carriers which are unexpected in a direct band-gap semiconductor [8–10]. The electronic band structure and the corresponding charge carrier dynamics are accessed by time- and angle-resolved photoelectron spectroscopy (ARPES) [8,9,11–23]. However, results from ARPES studies are partially conflicting [24,25]. One reason could be the lack of preparation methods to generate well-defined surfaces. ARPES is a surface-sensitive method so that surface properties influence results heavily. For example, if MHPs exhibit different surface terminations, those may alter the electronic surface structure drastically [26,27].

To improve the situation and reliability of MHP preparation and control of surfaces and interfaces, we present a refined preparation recipe for MHPs based on molecular beam epitaxy in ultrahigh vacuum. The inorganic perovskites $CsPbBr_3$ and $CsSnBr_3$ have a nearly cubic structure with lattice parameters of $a = 0.585$ and 0.579 nm, respectively. These are roughly twice as large as the lattice parameter of a Au(001) surface ($a_{Au} = 0.287$ nm). The lattice mismatches for a (2×2) superstructure on the Au(001) surface are only 1.9 % and 0.9 %, respectively. This facilitates the epitaxial growth of inorganic MHPs. Our approach generates well-defined MHP surfaces with (001) surface orientation, a tunable surface termination, and a very low defect density. The prepared $CsPbBr_3$ thin films are intrinsic semiconductors. We present a multimethod analysis of the surfaces, including scanning tunneling microscopy (STM), low-energy electron diffraction (LEED), and ultraviolet photoelectron spectroscopy (UPS) to determine the atomic and electronic surface structure of the epitaxial thin films.

II. EXPERIMENT

The experiments were performed in three different ultrahigh vacuum chambers, one of which was equipped with an STM operating at 80 K, the other with an STM operating at 295 K, and the third with a setup for UPS. Before each preparation, clean Au(001) surfaces were prepared by repeated Ne^+ bombardment with 1–2 keV energy and annealing to a maximum temperature of 970 K. Epitaxially grown $CsPb(Sn)Br_3$ films were prepared by thermal coevaporation of CsBr ($T_{evap} \approx 770$ K) and $PbBr_2$ ($T_{evap} \approx 600$ K) or $SnBr_2$ ($T_{evap} \approx 470$ K) (all three Sigma-Aldrich, 99% purity) from graphite crucibles of home-built dual-source Knudsen-cell type evaporators. Evaporation rates were calibrated individually with a quartz microbalance setting the growth rate at approximately 0.75 monolayers (ML) per minute. A monolayer is defined here as the amount of CsBr and $Pb(Sn)Br_2$ needed for one ML $CsPb(Sn)Br_3$, corresponding to a (2×2)
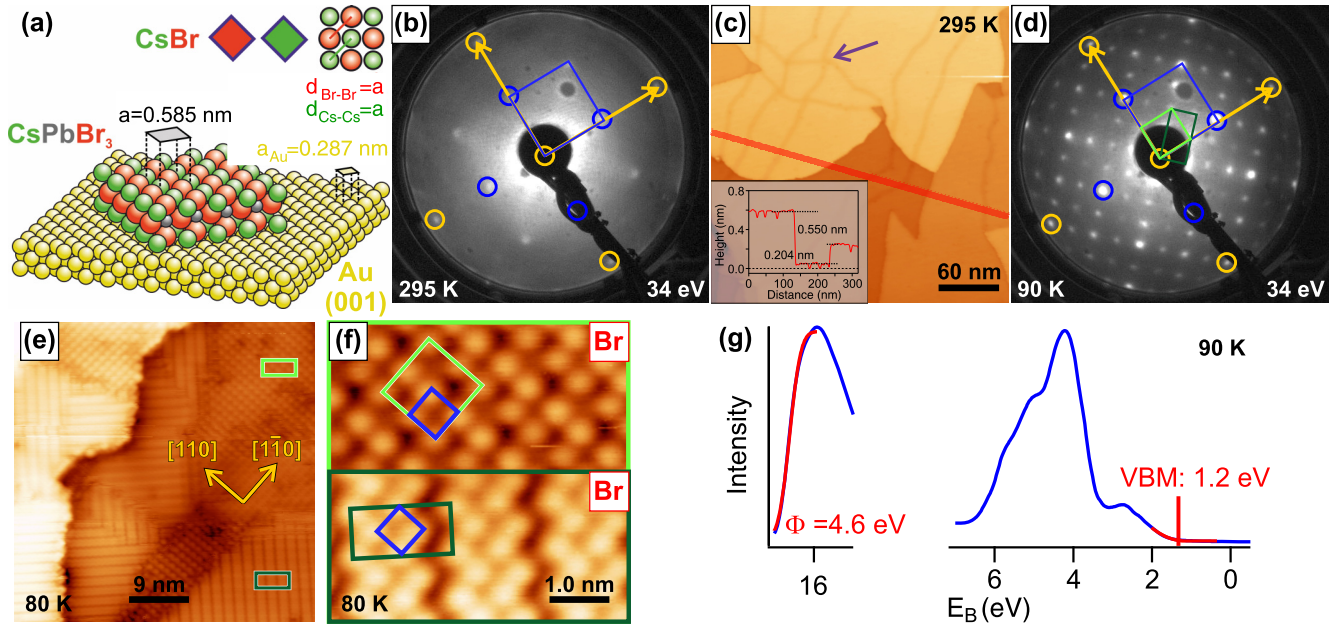
————
*thomas.fauster@fau.de

FIG. 1. Atomic and electronic structure of epitaxial CsBr-terminated CsPbBr$_3$(001) on Au(001). (a) Schematic illustration of the crystal lattice alignment. (b) LEED pattern. (c) Large-scale STM image (300 nm×300 nm) at 295 K. The inset shows a line scan along the red line indicated in the main panel. Panels (d) and (e) present a corresponding LEED pattern and an STM image (45 nm×45 nm) measured at 90 K and 80 K, respectively. (f) Atomically resolved (5 nm×2.5 nm) STM images at 80 K. The blue squares in panels (d) and (f) mark the (1×1) unit cell of CsPbBr$_3$, whereas the light and dark green rectangles in panel (f) indicate (2×2) and (2$\sqrt{2}$×$\sqrt{2}$)R45° supercells, respectively. STM parameters (tunneling voltage/current): (c) 3.5 V/0.22 nA, (e) 3.3 V/0.03 nA, and (f) 2.5 V/0.02 nA (top), 2.3 V/0.02 nA (bottom). (g) UPS results from the vacuum edge at large and the valence bands at low binding energies E_B, respectively. All investigated films had thicknesses between 8 and 14 ML.

superstructure on the Au(001) substrate. Films were prepared with a 1 : 1 stoichiometry of both components if not stated differently. The Au(001) substrate was kept at 420 K during the deposition of CsBr and PbBr$_2$ resulting in well-ordered CsPbBr$_3$ films. Optimal ordering of CsSnBr$_3$ is achieved by codeposition at 90 K and subsequent annealing to 410 K for 10 min. We prepared a fresh surface prior to any experiment and checked the sample quality by comparing the relative intensities of the LEED spots at selected beam energies, which gave consistent results upon preparation in any of the three chambers. LEED experiments were conducted using home-built three-grid LEED optics. STM at 80 K was carried out with a home-built setup and at 295 K with a beetle-type STM. The bias voltages given in this paper are the sample potential with respect to the tip. All UPS measurements were performed with unpolarized light with a photon energy of 21.2 eV (He I). The He I satellite lines were subtracted for the shown spectra. An ellipsoidal display-type analyzer with an energetic resolution of 100 meV was utilized to measure photoemission spectra [28]. All photoelectrons from an emission cone with an opening angle of 25° with respect to the surface normal were integrated for the presented UPS spectra.

III. RESULTS AND DISCUSSION

A. CsBr-terminated surface

The resulting atomic and electronic surface structures of epitaxially grown CsPbBr$_3$ films on Au(001) are shown in Fig. 1. Corresponding results from CsSnBr$_3$ are presented in the Supplemental Material [Fig. A1(a)] [29]. All epitaxial

CsPbBr$_3$ films with a film thickness larger than 6 ML show well-ordered surfaces as illustrated schematically in Fig. 1(a). Corresponding LEED patterns recorded at 295 K are shown in Fig. 1(b). The LEED spots in the blue circles correspond to the square (001) surface unit cell of the nearly cubic building block of the MHP ($a \approx 0.577$ nm) [30]. Yellow circles mark the nominal positions of the square unit cell of the bare Au(001) substrate. The LEED pattern proves the (2×2) epitaxial relation of the MHP with only one well-defined (001) surface orientation in which the [110] direction of the MHP crystal lattice is strictly aligned to the [110] direction of Au [compare Fig. 1(a)]. This agrees with calculations predicting a preferential (001) orientation of MHP surfaces [7,31–33]. The LEED pattern indicates a cubic (1×1) perovskite structure at 295 K, even though CsPbBr$_3$ should be in the orthorhombic phase below 380 K with characteristic superstructures when bulk-terminated [30]. We speculate that this anomaly is the result of an altered phase transition temperature in thin films compared to the bulk [34]. Anchoring to the substrate may shift the phase transition temperature as well [35].

Large-scale STM images [Fig. 1(c)] show flat films with grain sizes >100 nm. The line scan reveals step heights around 0.550 and 0.204 nm. The latter corresponds to the height difference between two terraces (0.203 nm) of the Au(001) substrate and is also observed in Figs. 1(e) and 1(d). The larger step height is close to the height of the CsPbBr$_3$ unit cell (0.585 nm). The discrepancy between the measured and geometric step height of CsPbBr$_3$ may be rationalized by different tunneling probabilities and consequently different tip sample distances due to the changed number of insulating
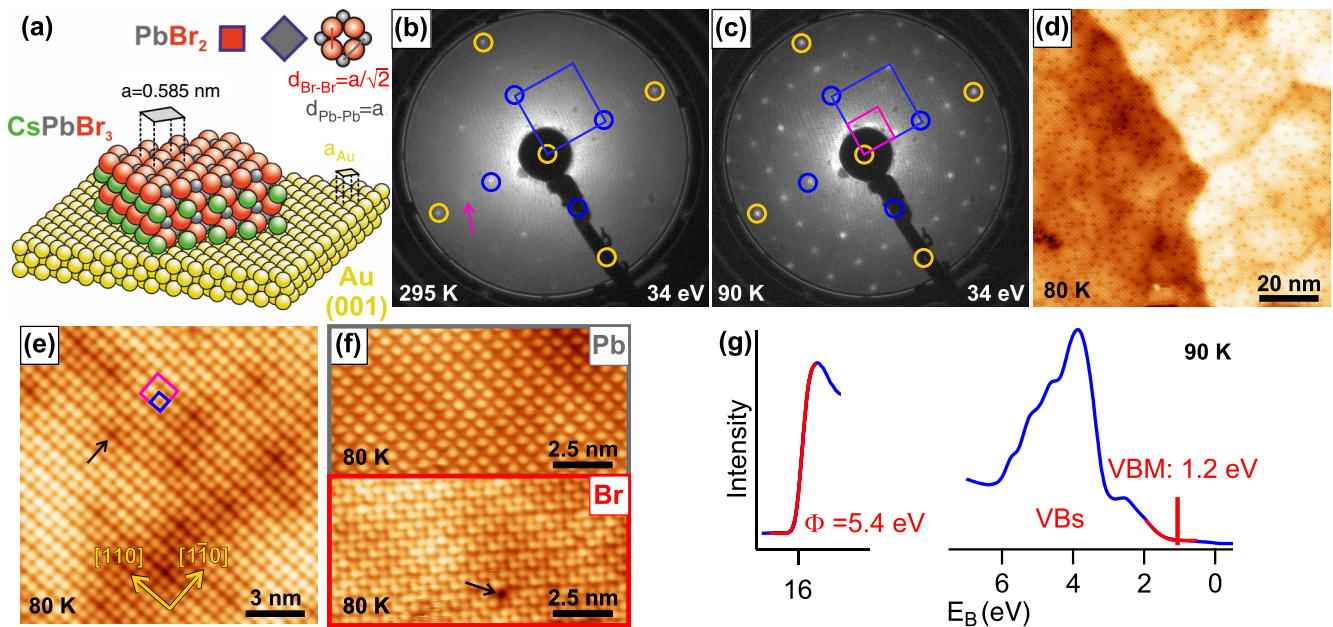
FIG. 2. Atomic and electronic surface structure of $PbBr_2$-terminated $CsPbBr_3(001)$ on Au(001). (a) Schematic illustration of the crystal lattice alignment. [(b), (c)] LEED patterns of 8 ML $CsPbBr_3(001)$ at 90 K and 295 K, respectively. [(d)–(f)] Corresponding large-scale (150×150 nm) and atomically resolved (15×15 nm and 12.5×6.25 nm) STM images. STM parameters (tunneling voltage/current): (d) 1.7 V/0.02 nA, (e) 1.6 V/0.02 nA, and (f) -1.3 V/0.02 nA (top), -1.5 V/0.02 nA (bottom). (g) UPS results of 14 ML $CsPbBr_3(001)$ from the vacuum edge at large and the valence bands at low binding energies E_B, respectively. The presented surfaces were prepared by adding 0.3–1 ML $PbBr_2$ onto a well-ordered MHP surface until the LEED pattern revealed a pure (2×2) reconstruction.

layers on the upper and lower terraces. Surface profiles show many more step heights related to Au(001) than to the MHP, indicating a homogeneous film thickness across the whole crystal surface. The surface exhibits shallow, stripe-shaped depressions [purple arrow in Fig. 1(c)] with an apparent depth of ≈ 0.1 nm. These stripes are only observed on films with thicknesses exceeding ≈ 6 ML. There is no dependency of stripe density on measurement temperature (compare Fig. 1 with Fig. A1(b) in the Supplemental Material [29]). Therefore, the stripes may be dislocations caused by relaxations in the bulk of thicker $CsPbBr_3$ films which reduce the epitaxial strain in $CsPbBr_3$ on Au(001).

Additional spots appear in the LEED pattern and the diffuse background is lowered if the temperature is decreased [see Fig. 1(d)]. Temperature-dependent LEED patterns are discussed in the Supplemental Material [Fig. A1(c)] [29]. By increasing the electron energy above 150 eV, the LEED spots disappear in the diffuse background. This process is reversible. STM images acquired with and without exposure of the sample to the electron beam did not show differences in the number and quality of defects. The vanishing of the diffraction spots accompanied by an increase of the background with temperature and electron energy is attributed to large vibration amplitudes of the soft MHP lattice. The LEED pattern in Fig. 1(d) at 90 K exhibits an overall c(4×4) superstructure with respect to the (001) unit cell of the MHP. Its origin can be elucidated by STM at 80 K. Figure 1(e) presents a (45 nm $\times 45$ nm) STM image in which two surface structures can be identified. One has a square shape (light green rectangle), while the other one shows an arrangement in stripes (dark green rectangle). They are caused by two distinct surface

reconstructions which can be identified in atomically resolved STM [see Fig. 1(f)]. Corresponding unit cells are indicated in light and dark green, exhibiting (2×2) and ($2\sqrt{2} \times \sqrt{2}$)R45° periodicities, respectively. The (2×2) reconstruction covers about 60% of the surface. These surface reconstructions were already observed on small CsBr-terminated $CsPbBr_3$ islands without long-range order [36]. They are caused by slight in-plane modulations of the positions of the imaged Br atoms [36–41]. A comparison to a second imaging mode with a functionalized STM tip is presented in Fig. A1(b) in the Supplemental Material [29], which proves the CsBr termination of the surface unambiguously. Our observation of a preferential CsBr termination is also consistent with previous measurements on other MHPs and various calculations for a 1 : 1 stoichiometry [33,36,38–40,42–47].

The electronic structure of the epitaxial thin films was investigated using UPS [Fig. 1(g)]. A work function of 4.6 ± 0.1 eV was determined from the cutoff (vacuum edge) at large binding energy E_B. This value is in line with theoretical expectations for a CsBr-terminated surface [36,43]. The valence band structure is detected between $E_B = 0$ eV and 6.5 eV [see Fig. 1(g)]. Three intense features can be found at $E_B = 4.2$ eV, $E_B = 5.0$ eV, and $E_B = 5.7$ eV, respectively. Those features are characteristic for the valence bands of MHPs and are typically observed in well-ordered samples like single crystals [13,14,18,19,24]. They are followed by the topmost valence bands at $E_B < 3$ eV. A half-parabola was fitted to the spectrum following a previous study [9] to determine the valence band maximum (VBM) at $E_B = 1.2 \pm 0.1$ eV. A comparison with the optical band gap of $E_{gap} = 2.25$ eV shows that our epitaxial thin films are almost intrinsic.

B. PbBr$_2$-terminated surface

The epitaxial growth of CsPbBr$_3$ with a $1:1$ ratio of supplied CsBr and PbBr$_2$ generates CsBr-terminated surfaces as shown in the previous section. This raises the question of whether the surface termination can be modified on purpose. Calculations predicted the possibility of PbBr$_2$-terminated surfaces if MHPs are prepared with an excess of PbBr$_2$ [33,46]. Our approach allows us to control the preferential surface structure in two ways. One way is to prepare samples with an excess of PbBr$_2$ ($\approx 10\%$ for 10 ML). The other is to evaporate additional PbBr$_2$ onto a well-ordered CsBr-terminated surface. Both approaches result in a surface structure as illustrated in Fig. 2(a) deviating from the surface with CsBr termination in Fig. 1(a). While interatomic distances d between Cs and Pb atoms are identical to the lattice parameter a for both terminations the interatomic distance d_{Br-Br} of the Br atoms is smaller by a factor of $1/\sqrt{2}$ for the Br-terminated surface.

The LEED data in Figs. 2(b) and 2(c) were taken at the same electron energy as for Figs. 1(b) and 1(d) but the overall appearance deviates markedly. This proves that the atomic surface structure of the two films is not the same. The LEED pattern of the PbBr$_2$-treated film at 295 K shows the (1×1) cell of the MHP as before [marked in blue, Figs. 2(b) and 2(c)]. In addition, an overall weak (2×2) superstructure (pink arrow) can be identified. It is the only superstructure for temperatures down to 90 K [Fig. 2(c)], unlike on the CsBr-terminated surface [Fig. 1(d)].

The large-scale STM image in Fig. 2(d) shows a long-range periodic structure with point defects (dark spots) at a density of 0.065 nm^{-2}, whose appearance depends strongly on the bias voltage. No grain boundaries can be detected on the 100-nm scale. The surface exhibits stripes with a comparable density and appearance as for the CsBr-terminated surface [see Fig. 1(c)].

We carried out atomically resolved STM to further analyze this surface structure. STM with a positive voltage between tip and sample finds a square surface unit cell with a (2×2) reconstruction (pink) in line with the LEED results [see Fig. 2(e)]. This configuration probes the unoccupied states of the sample (mainly from Pb-$6p$ orbitals at the conduction band minimum) [18] by tunneling electrons from the tip into the sample. The average distance between the imaged protrusions is 0.57 ± 0.02 nm as expected for Pb atoms in a PbBr$_2$-terminated surface. Point defects on the surface are imaged as cross-like depressions (indicated by a black arrow).

The occupied states of the sample (mainly from Br-$4p$ and Pb-$6s$ orbitals at the VBM of CsPbBr$_3$ [18]) can be probed applying a negative voltage to the sample. The STM tip tends to interact with the sample in this configuration so that it gets functionalized spontaneously. Results from two different imaging modes recorded with comparable negative voltages are presented in Fig. 2(f). The first imaging mode detects an average distance of 0.57 ± 0.02 nm between the imaged

protrusions and a (2×2) surface reconstruction consistent with previous results [top image in Fig. 2(f)]. However, the second mode images twice as many protrusions [bottom image in Fig. 2(f)]. The spacing between these species is reduced by a factor of $\sqrt{2}$. The corresponding surface unit cell is rotated by 45° in comparison to the unit cell observed before (indicated by a light blue square). This proves unambiguously a PbBr$_2$-terminated surface since such behavior is only possible for the Pb and Br atoms in a PbBr$_2$ termination, respectively [compare Fig. 2(a)]. The observed point defects on the PbBr$_2$-terminated surface stem from Br vacancies consistent with earlier observations [40].

Finally, we discuss the electronic surface structure of the PbBr$_2$-terminated surface [see Fig. 2(g)]. The VBM is located at $E_B = 1.2$ eV as for the CsBr-terminated surface. Thus, the PbBr$_2$ excess does not dope the sample indicating negligible changes in the CsPbBr$_3$ bulk. The only observable difference between both terminations is the significantly increased work function of the PbBr$_2$-terminated surface with $\Phi = 5.3 \pm 0.1$ eV. Such an increase of ≈ 0.7 eV is expected for a PbBr$_2$-terminated surface [31,43,48]. It is also in line with the increasing work function of polycrystalline thin films with increasing PbBr$_2$ content [49].

IV. SUMMARY AND CONCLUSIONS

In summary, we demonstrated the epitaxial growth of (001)-oriented CsPbBr$_3$ and CsSnBr$_3$ thin films on Au(001) with domain sizes exceeding $(100 \text{ nm})^2$. The CsPbBr$_3$ thin films are intrinsic semiconductors, in contrast to polycrystalline MHP thin films and single crystals [18,19,50]. Stochiometric films are CsBr terminated and exhibit characteristic (2×2) and $(2\sqrt{2}\times\sqrt{2})$R45° surface reconstructions. Their work function is $\Phi = 4.6 \pm 0.1$ eV. A surplus of PbBr$_2$ during growth or postdeposition of PbBr$_2$ creates PbBr$_2$-terminated (001) surfaces with a (2×2) surface reconstruction and a higher work function of $\Phi = 5.3 \pm 0.1$ eV. Our work opens a route to create well-ordered MHPs with the option to control the film thickness and surface termination layer by layer. This enables a detailed investigation and tuning of the surface electronic structure at interfaces which is a prerequisite for understanding band alignment schemes, surface carrier dynamics, and diffusion in MHP devices [51]. The change in work function with surface termination has drastic consequences for band alignments at interfaces that remain obscured if different terminations are present in samples or devices [2].

[1] L. Schmidt-Mende, V. Dyakonov, S. Olthof, F. Ünlü, K. M. T. Lê, S. Mathur, A. D. Karabanov, D. C. Lupascu, L. M. Herz, A. Hinderhofer, F. Schreiber, A. Chernikov, D. A. Egger, O. Shargaieva, C. Cocchi, E. Unger, M. Saliba, M. M. Byranvand,

M. Kroll, F. Nehm *et al.*, Roadmap on organic-inorganic hybrid perovskite semiconductors and devices, APL Mater. **9**, 109202 (2021).

[2] P. Schulz, D. Cahen, and A. Kahn, Halide perovskites: Is it all about the interfaces? Chem. Rev. **119**, 3349 (2019).

[3] H. Jin, E. Debroye, M. Keshavarz, I. G. Scheblykin, M. B. Roeffaers, J. Hofkens, and J. A. Steele, It's a trap! On the nature of localised states and charge trapping in lead halide perovskites, Mater. Horiz. **7**, 397 (2020).

[4] S. Y. Leblebici, L. Leppert, Y. Li, S. E. Reyes-Lillo, S. Wickenburg, E. Wong, J. Lee, M. Melli, D. Ziegler, D. K. Angell, D. F. Ogletree, P. Ashby, F. M. Toma, J. B. Neaton, I. D. Sharp, and A. Weber-Bargioni, Facet-dependent photovoltaic efficiency variations in single grains of hybrid halide perovskite, Nat. Energy **1**, 16093 (2016).

[5] C. Ma, M. Grätzel, and N.-G. Park, Facet engineering for stable, efficient perovskite solar cells, ACS Energy Lett. **7**, 3120 (2022).

[6] F. Zu, D. Shin, and N. Koch, Electronic properties of metal halide perovskites and their interfaces: The basics, Mater. Horiz. **9**, 17 (2022).

[7] A. Buin, P. Pietsch, J. Xu, O. Voznyy, A. H. Ip, R. Comin, and E. H. Sargent, Materials processing routes to trap-free halide perovskites, Nano Lett. **14**, 6281 (2014).

[8] D. Niesner, H. Zhu, K. Miyata, P. P. Joshi, T. J. Evans, B. J. Kudisch, M. T. Trinh, M. Marks, and X.-Y. Zhu, Persistent energetic electrons in methylammonium lead iodide perovskite thin films, J. Am. Chem. Soc. **138**, 15717 (2016).

[9] D. Niesner, M. Wilhelm, I. Levchuk, A. Osvet, S. Shrestha, M. Batentschuk, C. Brabec, and T. Fauster, Giant Rashba Splitting in $CH_3NH_3PbBr_3$ Organic-Inorganic Perovskite, Phys. Rev. Lett. **117**, 126401 (2016).

[10] F. Wang, Y. Fu, M. E. Ziffer, Y. Dai, S. F. Maehrlein, and X.-Y. Zhu, Solvated electrons in solids-ferroelectric large polarons in lead halide perovskites, J. Am. Chem. Soc. **143**, 5 (2021).

[11] C. Wang, B. R. Ecker, H. Wei, J. Huang, J.-Q. Meng, and Y. Gao, Valence band dispersion measurements of perovskite single crystals using angle-resolved photoemission spectroscopy, Phys. Chem. Chem. Phys. **19**, 5361 (2017).

[12] T. Komesu, X. Huang, T. R. Paudel, Y. B. Losovyj, X. Zhang, E. F. Schwier, Y. Kojima, M. Zheng, H. Iwasawa, K. Shimada, M. I. Saidaminov, D. Shi, A. L. Abdelhady, O. M. Bakr, S. Dong, E. Y. Tsymbal, and P. A. Dowben, Surface electronic structure of hybrid organolead bromide perovskite single crystals, J. Phys. Chem. C **120**, 21710 (2016).

[13] M.-I. Lee, A. Barragán, M. N. Nair, V. L. R. Jacques, D. L. Bolloc'h, P. Fertey, K. Jemli, F. Lédée, G. Trippé-Allard, E. Deleporte, A. Taleb-Ibrahimi, and A. Tejeda, First determination of the valence band dispersion of $CH_3NH_3PbI_3$ hybrid organic–inorganic perovskite, J. Phys. D: Appl. Phys. **50**, 26LT02 (2017).

[14] J.-P. Yang, M. Meissner, T. Yamaguchi, X.-Y. Zhang, T. Ueba, L.-W. Cheng, S. Ideta, K. Tanaka, X.-H. Zeng, N. Ueno, and S. Kera, Band dispersion and hole effective mass of methylammonium lead iodide perovskite, Solar RRL **2**, 1800132 (2018).

[15] T. J. Evans, K. Miyata, P. P. Joshi, S. Maehrlein, F. Liu, and X.-Y. Zhu, Competition between hot-electron cooling and large polaron screening in $CsPbBr_3$ perovskite single crystals, J. Phys. Chem. C **122**, 13724 (2018).

[16] F. Zu, P. Amsalem, D. A. Egger, R. Wang, C. M. Wolff, H. Fang, M. A. Loi, D. Neher, L. Kronik, S. Duhm, and N. Koch, Constructing the electronic structure of $CH_3NH_3PbI_3$ and $CH_3NH_3PbBr_3$ perovskite thin films from single-crystal band structure measurements, J. Phys. Chem. Lett. **10**, 601 (2019).

[17] P. Nandi, S. K. Pandey, C. Giri, V. Singh, L. Petaccia, U. Manju, S. D. Mahanti, and D. Topwal, Probing the electronic structure of hybrid perovskites in the orientationally disordered cubic phase, J. Phys. Chem. Lett. **11**, 5719 (2020).

[18] M. Puppin, S. Polishchuk, N. Colonna, A. Crepaldi, D. N. Dirin, O. Nazarenko, R. De Gennaro, G. Gatti, S. Roth, T. Barillot, L. Poletto, R. P. Xian, L. Rettig, M. Wolf, R. Ernstorfer, M. V. Kovalenko, N. Marzari, M. Grioni, and M. Chergui, Evidence of Large Polarons in Photoemission Band Mapping of the Perovskite Semiconductor $CsPbBr_3$, Phys. Rev. Lett. **124**, 206402 (2020).

[19] D. Niesner, Surface electronic structure and dynamics of lead halide perovskites, APL Mater. **8**, 090704 (2020).

[20] E. Jung, K. Budzinauskas, S. Öz, F. Ünlü, H. Kuhn, J. Wagner, D. Grabowski, B. Klingebiel, M. Cherasse, J. Dong, A. Pierfrancesco, P. Vivo, T. Kirchartz, T. Miyasaka, P. van Loosdrecht, L. Perfetii, and M. Sanjay, Femto- to microsecond dynamics of excited electrons in a quadruple cation perovskite, ACS Energy Lett. **5**, 785 (2020).

[21] J. Yang, H. Sato, H. Orio, X. Liu, M. Fahlman, N. Ueno, H. Yoshida, T. Yamada, and S. Kera, Accessing the conduction band dispersion in $CH_3NH_3PbI_3$ single crystals, J. Phys. Chem. Lett. **12**, 3773 (2021).

[22] S. Polishchuk, M. Puppin, A. Crepaldi, G. Gatti, D. N. Dirin, O. Nazarenko, N. Colonna, N. Marzari, M. V. Kovalenko, M. Grioni, and M. Chergui, Nanoscale-resolved surface-to-bulk electron transport in $CsPbBr_3$ perovskite, Nano Lett. **22**, 1067 (2022).

[23] M. Cherasse, J. Dong, G. Trippé-Allard, E. Deleporte, D. Garrot, S. F. Maehrlein, M. Wolf, Z. Chen, E. Papalazarou, M. Marsi, J.-P. Rueff, A. Taleb-Ibrahimi, and L. Perfetti, Electron dynamics in hybrid perovskites reveal the role of organic cations on the screening of local charges, Nano Lett. **22**, 2065 (2022).

[24] M. Sajedi, M. Krivenkov, D. Marchenko, A. Varykhalov, J. Sánchez-Barriga, E. D. L. Rienks, and O. Rader, Absence of a giant Rashba effect in the valence band of lead halide perovskites, Phys. Rev. B **102**, 081116(R) (2020).

[25] M. Sajedi, M. Krivenkov, D. Marchenko, J. Sánchez-Barriga, A. K. Chandran, A. Varykhalov, E. D. L. Rienks, I. Aguilera, S. Blügel, and O. Rader, Is there a Polaron Signature in Angle-Resolved Photoemission of $CsPbBr_3$? Phys. Rev. Lett. **128**, 176405 (2022).

[26] E. Mosconi, T. Etienne, and F. De Angelis, Rashba band splitting in organohalide lead perovskites: Bulk and surface effects, J. Phys. Chem. Lett. **8**, 2247 (2017).

[27] J. Yang, M. Meissner, T. Yamaguchi, B. Xi, K. Takahashi, S. A. A. Rahman, X. Liu, H. Yoshida, M. Fahlman, and S. Kera, Temperature-dependent band structure evolution determined by surface geometry in organic halide perovskite single crystals, Phys. Rev. B **102**, 245101 (2020).

[28] D. Rieger, R. Schnell, W. Steinmann, and V. Saile, A display-type analyzer with an image-processing system for angle-resolved photoelectron spectroscopy, Nucl. Instrum. Methods Phys. Res. **208**, 777 (1983).

[29] See Supplemental Material at http://link.aps.org/supplemental/10.1103/PhysRevMaterials.7.035403 for measurements on CsSnPb$_3$, details of the STM imaging modes, and temperature-dependent data (see also Refs. [52–56] therein).

[30] C. C. Stoumpos, C. D. Malliakas, J. A. Peters, Z. Liu, M. Sebastian, J. Im, T. C. Chasapis, A. C. Wibowo, D. Y. Chung, A. J. Freeman, B. W. Wessels, and M. G. Kanatzidis, Crystal growth of the perovskite semiconductor CsPbBr$_3$: A new material for high-energy radiation detection, Cryst. Growth Des. **13**, 2722 (2013).

[31] Y.-K. Jung, K. T. Butler, and A. Walsh, Halide perovskite heteroepitaxy: Bond formation and carrier confinement at the PbS–CsPbBr$_3$ interface, J. Phys. Chem. C **121**, 27351 (2017).

[32] J. Hieulle, C. Stecker, R. Ohmann, L. K. Ono, and Y. Qi, Scanning probe microscopy applied to organic-inorganic halide perovskite materials and solar cells, Small Methods **2**, 1700295 (2018).

[33] Y. Yang, C. Hou, and T.-X. Liang, Energetic and electronic properties of CsPbBr$_3$ surfaces: A first-principles study, Phys. Chem. Chem. Phys. **23**, 7145 (2021).

[34] D. Li, G. Wang, H.-C. Cheng, C.-Y. Chen, H. Wu, Y. Liu, Y. Huang, and X. Duan, Size-dependent phase transition in methylammonium lead iodide perovskite microplate crystals, Nat. Commun. **7**, 11330 (2016).

[35] M. Sytnyk, A.-A. Yousefi-Amin, T. Freund, A. Prihoda, K. Götz, T. Unruh, C. Harreiss, J. Will, E. Spiecker, J. Levchuk, A. Osvet, C. J. Brabec, U. Künecke, P. Wellmann, V. V. Volobuev, J. Korczak, A. Szczerbakow, T. Story, C. Simbrunner, G. Springholz *et al.*, Epitaxial metal halide perovskites by inkjet-printing on various substrates, Adv. Funct. Mater. **30**, 2004612 (2020).

[36] J. Hieulle, S. Luo, D.-Y. Son, A. Jamshaid, C. Stecker, Z. Liu, G. Na, D. Yang, R. Ohmann, L. K. Ono, L. Zhang, and Y. Qi, Imaging of the atomic structure of all-inorganic halide perovskites, J. Phys. Chem. Lett. **11**, 818 (2020).

[37] R. Ohmann, L. K. Ono, H.-S. Kim, H. Lin, M. V. Lee, Y. Li, N.-G. Park, and Y. Qi, Real-space imaging of the atomic structure of organic-inorganic perovskite, J. Am. Chem. Soc. **137**, 16049 (2015).

[38] L. She, M. Liu, and D. Zhong, Atomic structures of CH$_3$NH$_3$PbI$_3$ (001) surfaces, ACS Nano **10**, 1126 (2016).

[39] J. Hieulle, X. Wang, C. Stecker, D.-Y. Son, L. Qiu, R. Ohmann, L. K. Ono, A. Mugarza, Y. Yan, and Y. Qi, Unraveling the impact of halide mixing on perovskite stability, J. Am. Chem. Soc. **141**, 3515 (2019).

[40] C. Stecker, K. Liu, J. Hieulle, R. Ohmann, Z. Liu, L. K. Ono, G. Wang, and Y. Qi, Surface defect dynamics in organic-inorganic hybrid perovskites: From mechanism to interfacial properties, ACS Nano **13**, 12127 (2019).

[41] H.-C. Hsu, B.-C. Huang, S.-C. Chin, C.-R. Hsing, D.-L. Nguyen, M. Schnedler, R. Sankar, R. E. Dunin-Borkowski, C.-M. Wei, C.-W. Chen, P. Ebert, and Y.-P. Chiu, Photodriven dipole reordering: Key to carrier separation in metal-organic halide perovskites, ACS Nano **13**, 4402 (2019).

[42] W. Geng, C.-J. Tong, Z.-K. Tang, C. Yam, Y.-N. Zhang, W.-M. Lau, and L.-M. Liu, Effect of surface composition on electronic properties of methylammonium lead iodide perovskite, J. Materiomics **1**, 213 (2015).

[43] X. Huang, T. R. Paudel, P. A. Dowben, S. Dong, and E. Y. Tsymbal, Electronic structure and stability of the CH$_3$NH$_3$PbBr$_3$ (001) surface, Phys. Rev. B **94**, 195309 (2016).

[44] Y. Yu, D. Zhang, C. Kisielowski, L. Dou, N. Kornienko, Y. Bekenstein, A. B. Wong, A. P. Alivisatos, and P. Yang, Atomic resolution imaging of halide perovskites, Nano Lett. **16**, 7530 (2016).

[45] L. She, M. Liu, X. Li, Z. Cai, and D. Zhong, Growth and interfacial structure of methylammonium lead iodide thin films on Au (111), Surf. Sci. **656**, 17 (2017).

[46] Z.-L. Yu, Q.-R. Ma, Y.-Q. Zhao, B. Liu, and M.-Q. Cai, Surface termination—a key factor to influence electronic and optical properties of CsSnI$_3$, J. Phys. Chem. C **122**, 9275 (2018).

[47] A. Mirzehmet, T. Ohtsuka, S. A. Abd. Rahman, T. Yuyama, P. Krüger, and H. Yoshida, Surface termination of solution-processed CH$_3$NH$_3$PbI$_3$ perovskite film examined using electron spectroscopies, Adv. Mater. **33**, 2004981 (2021).

[48] C. Quarti, F. De Angelis, and D. Beljonne, Influence of surface termination on the energy level alignment at the CH$_3$NH$_3$PbI$_3$ perovskite/C60 interface, Chem. Mater. **29**, 958 (2017).

[49] J. Emara, T. Schnier, N. Pourdavoud, T. Riedl, K. Meerholz, and S. Olthof, Impact of film stoichiometry on the ionization energy and electronic structure of CH$_3$NH$_3$PbI$_3$ perovskites, Adv. Mater. **28**, 553 (2016).

[50] J. Endres, D. A. Egger, M. Kulbak, R. A. Kerner, L. Zhao, S. H. Silver, G. Hodes, B. P. Rand, D. Cahen, L. Kronik, and A. Kahn, Valence and conduction band densities of states of metal halide perovskites: A combined experimental–theoretical study, J. Phys. Chem. Lett. **7**, 2722 (2016).

[51] J. Rieger, J. Hauner, D. Niesner, and T. Fauster, Surface carrier dynamics and diffusion in inorganic metal-halide perovskite films, Phys. Rev. B **107**, 125205 (2023).

[52] D. H. Fabini, G. Laurita, J. S. Bechtel, C. C. Stoumpos, H. A. Evans, A. G. Kontos, Y. S. Raptis, P. Falaras, A. Van der Ven, M. G. Kanatzidis, and R. Seshadri, Dynamic stereochemical activity of the Sn^{2+} lone pair in perovskite CsSnBr$_3$, J. Am. Chem. Soc. **138**, 11820 (2016).

[53] H. A. Schwartz, H. Laurenzen, A. Marzouk, M. Runkel, K. O. Brinkmann, D. Rogalla, T. Riedl, S. Ashhab, and S. Olthof, Band-gap tuning in all-inorganic CsPb$_x$Sn$_{1-x}$Br$_3$ perovskites, ACS Appl. Mater. Interfaces **13**, 4203 (2021).

[54] K. Heidrich, W. Schäfer, M. Schreiber, J. Söchtig, G. Trendel, J. Treusch, T. Grandke, and H. J. Stolz, Electronic structure, photoemission spectra, and vacuum-ultraviolet optical spectra of CsPbCl$_3$ and CsPbBr$_3$, Phys. Rev. B **24**, 5642 (1981).

[55] M. Kamada, O. Aita, K. Ichikawa, M. Okusawa, and K. Tsutsumi, Photoelectron spectroscopic study of the decay process of excited 4d states in cesium halides, Phys. Rev. B **45**, 12725 (1992).

[56] M. Schmid, H.-P. Steinrück, and J. M. Gottfried, A new asymmetric pseudo-Voigt function for more efficient fitting of XPS lines, Surf. Interface Anal. **46**, 505 (2014).